Emergent topological spin structures in centrosymmetric cubic perovskite $SrFeO_3$

S. Ishiwata,* T. Nakajima, J.-H. Kim, D. S. Inosov, N. Kanazawa,
J. S. White, J. L. Gavilano, R. Georgii, K. Seemann, G. Brandl,
P. Manuel, D. D. Khalyavin, S. Seki, Y. Tokunaga, M. Kinoshita,
Y. W. Long, Y. Kaneko, Y. Taguchi, T. Arima, B. Keimer, and Y. Tokura

Correspondence to: ishiwata@mp.es.osaka-u.ac.jp

Details on magnetic structure and domain in Phase I

To check the presence of the $\boldsymbol{q}$-dependent domains in Phase I, we measured the magnetic scattering intensities along the three <111> equivalents, [1-1-1], [-11-1], and [-1-11] at 3 K as shown in Figs. S2(a) and S2(b). These data were collected by rotating the sample around the ω axis (parallel to [111]) in the vertical configuration (See Figs. S1(b) and S1(d)). The magnetic scattering intensities are significantly different not only after the zero-field cooling (ZFC) process (Fig. S2(a)) but after the field-cooling (FC) process (Fig. S2(b)). This result signifies the imbalance of the $\boldsymbol{q}$-dependent domains of the anisotropic double-$\boldsymbol{q}$ state in Phase I even after the FC process.

The peak splitting around $\boldsymbol{q}_1$ after FC in Phase I as seen in Fig. 3(e) was also observed for $\boldsymbol{q}_{1\text{-}4}$, i.e., for all <111> equivalents, after ZFC. However, the peak splitting in Phase I after ZFC is more complicated than that after FC because of the larger number of the domain types. As summarized in Table S1, there are 12 kinds of $\boldsymbol{q}$-dependent domains of the anisotropic double-$\boldsymbol{q}$ helimagnetic structure (there exist 48 kinds of helimagnetic domains, when considering the spin helicity degree of freedom for each of the $\boldsymbol{q}$-vector). After the FC process, there remain 3 kinds of $\boldsymbol{q}$-dependent domains named (1p, 2c), (1p, 3c), and (1p, 4c), of which proper-screw spin components with propagation vectors of $\boldsymbol{q}'_{1(2)}$, $\boldsymbol{q}'_{1(3)}$, $\boldsymbol{q}'_{1(4)}$, respectively, afford three scattering peaks on the (111) plane as shown in Fig. 3(e) (see also Figs. 3(a) and 3(c)). On the other hand, after the ZFC process, 6 out of the 12 kinds of $\boldsymbol{q}$-dependent domains contribute to the magnetic reflections around each of $\boldsymbol{q}_{1\text{-}4}$. For instance, there are 6 magnetic reflections near the reciprocal lattice position of $(-q,-q,q)$ $(=\boldsymbol{q}_2)$, as schematically shown in Fig. S5(a). This situation was verified by the WISH experiment at 50 K after ZFC. The diffraction profiles around $\boldsymbol{q}_2$ as a function of d-spacing show that each of the three split peaks observed after FC is further split into two components with different d-spacing, 17.4 Å and 17.9 Å, as shown in Figs. S5(b)-(d). The peak splitting along $\boldsymbol{q}'_2$ manifests itself as the difference in the modulation periods for the proper-screw and cycloidal spin components in the double-$\boldsymbol{q}$ helimagnetic structure and the detection of the 6 kinds of $\boldsymbol{q}$-dependent domains (2p, 1c), (2p, 3c), (2p, 4c), (1p, 2c), (3p, 2c), and (4p, 2c). Considering the fact that only the component of the magnetic moments perpendicular to the scattering vector (or the helimagnetic $\boldsymbol{q}$ vector) causes neutron scattering, the strong peaks at 17.9 Å and the small peaks at 17.4 Å in Figs. S5(b)-(d) are attributable to the proper screw and the cycloidal spin components, respectively.

Figures S6(a)-(c) show the field variations of the magnetic scattering profiles near the reciprocal lattice position of (-q,-q,q) (=$\boldsymbol{q}_2$) in Phase I. As the magnetic field increases beyond 4 T, where the proper-screw spin component is supposed to be fully aligned along the field direction, only the reflection from the cycloidal spin component of the domain (1p, 2c) becomes dominant and the all the others tend to disappear. This behavior can be interpreted as the field-induced alignment of the $\boldsymbol{q}$-dependent domains (see Fig. S6(d)), supporting the presumption that the proper-screw and cycloid spin components have slightly longer and shorter modulation periods, respectively. The rearrangement of the double-$\boldsymbol{q}$ magnetic domains can also be seen at the satellite reflections near the reciprocal lattice point of (1,-1,0), as shown in Fig. S3(b). Although the sixfold splitting of the magnetic peak was not resolved in these diffraction profiles, we found that the widths of the peaks were significantly changed by applying magnetic fields along the [111] direction. In particular, the reflections of $\boldsymbol{q}_2$, $\boldsymbol{q}_3$, and $\boldsymbol{q}_4$ became sharper at 8 T, because only one magnetic peak was left at each reciprocal lattice position, as illustrated in Fig. S6(d).

The coexistence of the two different magnetic propagation vectors should lower the symmetry of the system. Among 48 symmetry elements belonging to the original space group of *Pm*-3*m*, only four of them are compatible with the anisotropic double-$\boldsymbol{q}$ model proposed in the present manuscript as shown in Table S2, suggesting that the symmetry of the system is reduced to triclinic (1) in Phase I.

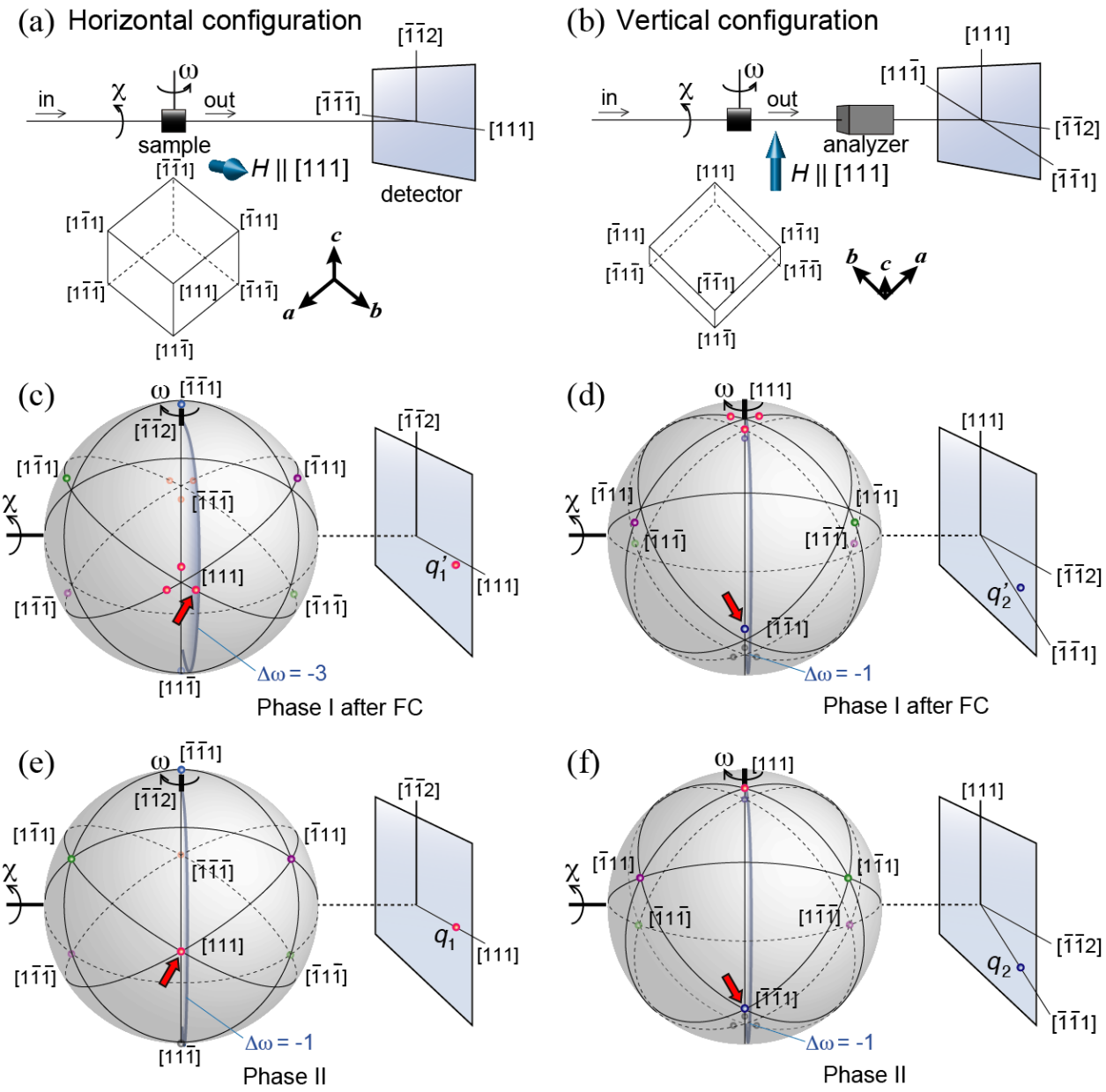

FIG. S1

(a) Experimental setup for horizontal magnetic field configuration. The applied field is perpendicular to the ω axis and parallel to [111]. (b) Experimental setup for vertical magnetic field configuration. The applied field is parallel to the ω axis and [111]. The analyzer was attached for measurements with a spin polarized mode. The cubic unit cells with Miller indices are shown for each configuration. (c)-(f) Schematic representations describing the relation between the crystallographic directions, the azimuthal positions of magnetic scattering peaks, the external magnetic field, and the neutron beam in Phase I after field cooling (FC) ((c)(d)) and Phase II ((e)(f)) in the horizontal configuration ((c)(e)) and the vertical configuration ((d)(f)). The points on each sphere represent the magnetic scattering peaks. The red arrow in each schematic representation indicates the scattering peak which appears in the detector.

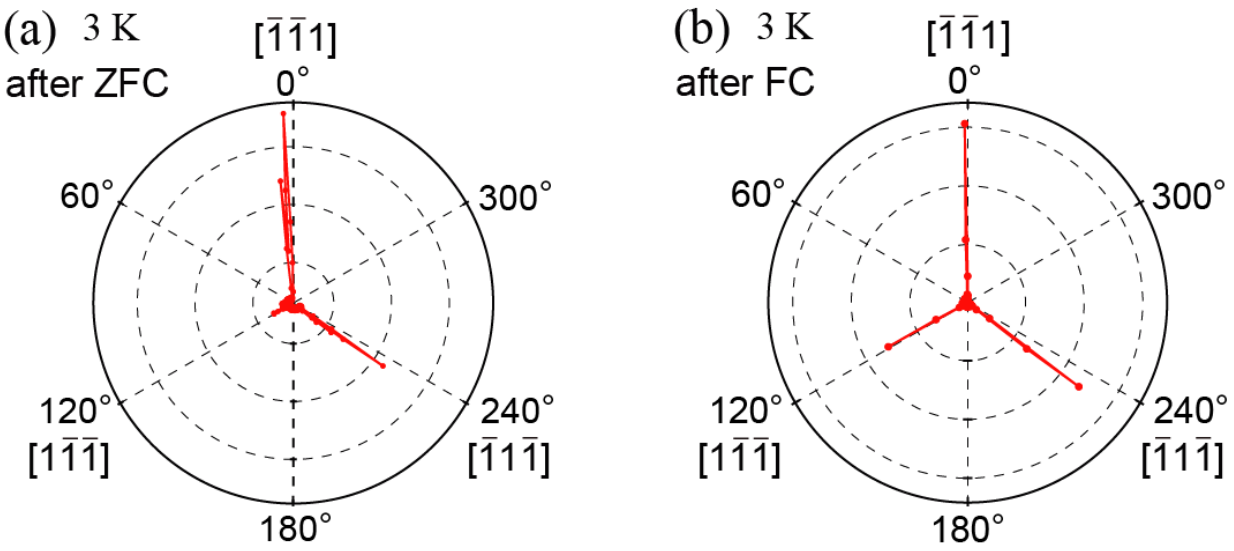

FIG. S2

Polar plot for the neutron scattering profile scanning the magnetic reflections of $\boldsymbol{q}_2$ along [1-1-1], [-11-1], and [-1-11] plotted as a function of the rotation angle ω around [111]. The data were measured at 3 K after (a) ZFC and (b) FC in the vertical magnetic field configuration.

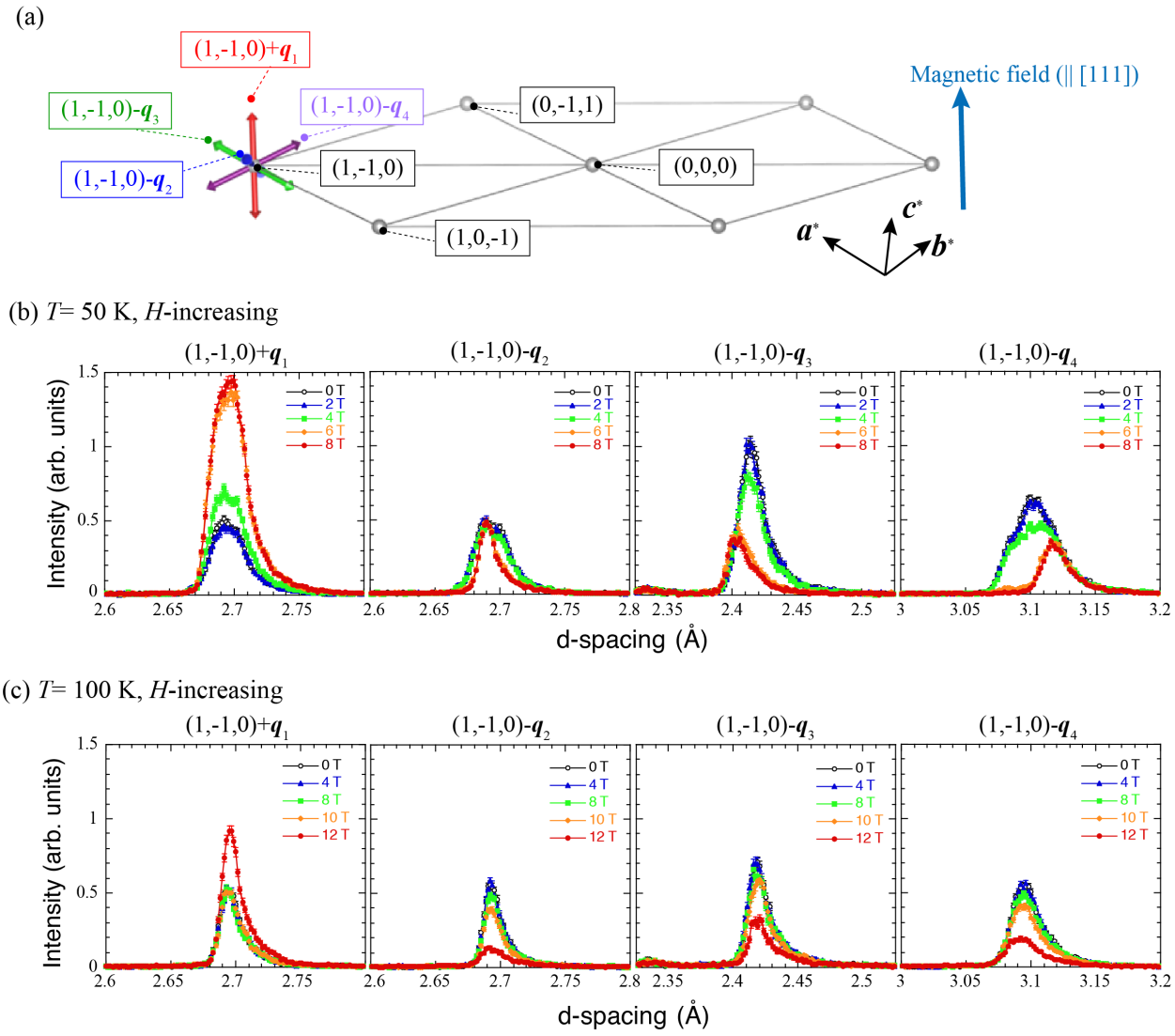

FIG. S3

(a) Schematic showing the directions of the external magnetic field and the ***q***-vectors of Phases I and II. Neutron diffraction profiles as a function of *d*-spacing for the magnetic reflections around ***Q***=(1,-1,0) measured with increasing field after ZFC at (b) 50 K and (c) 100 K. *d*-spacing is defined as $2\pi/Q$, where Q is a momentum transfer of neutron when measuring the satellite magnetic reflection.

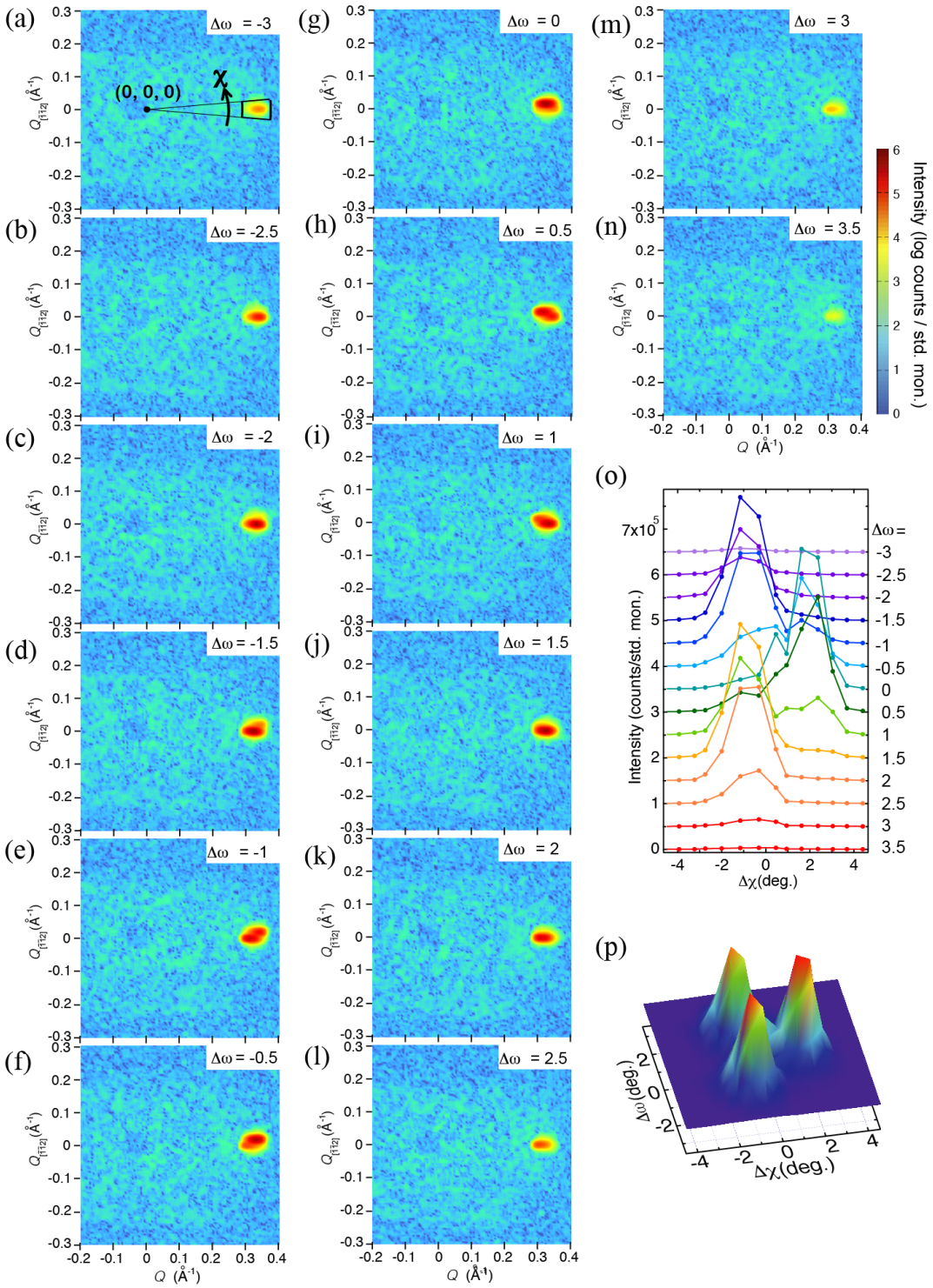

FIG. S4

(a-n) SANS data for the magnetic reflections for $\boldsymbol{q}_1$ along [111] at 3 K after FC. The relative rocking angle Δω was changed from (a) -3 through (n) 3.5 by 0.5 degree (For the experimental setup, see Figs. S1(a) and (c)). (o) Integrated scattering intensity as a function of Δχ for each relative rocking angle Δω. For instance, the scattering profile for each Δω is obtained by the integration at each Δχ as a function of Q in the range $0.28 \leq Q \leq 0.38$. (p) Neutron scattering profile as functions of Δω and Δχ obtained from the data set of (o). This profile is identical to Fig. 3(e).

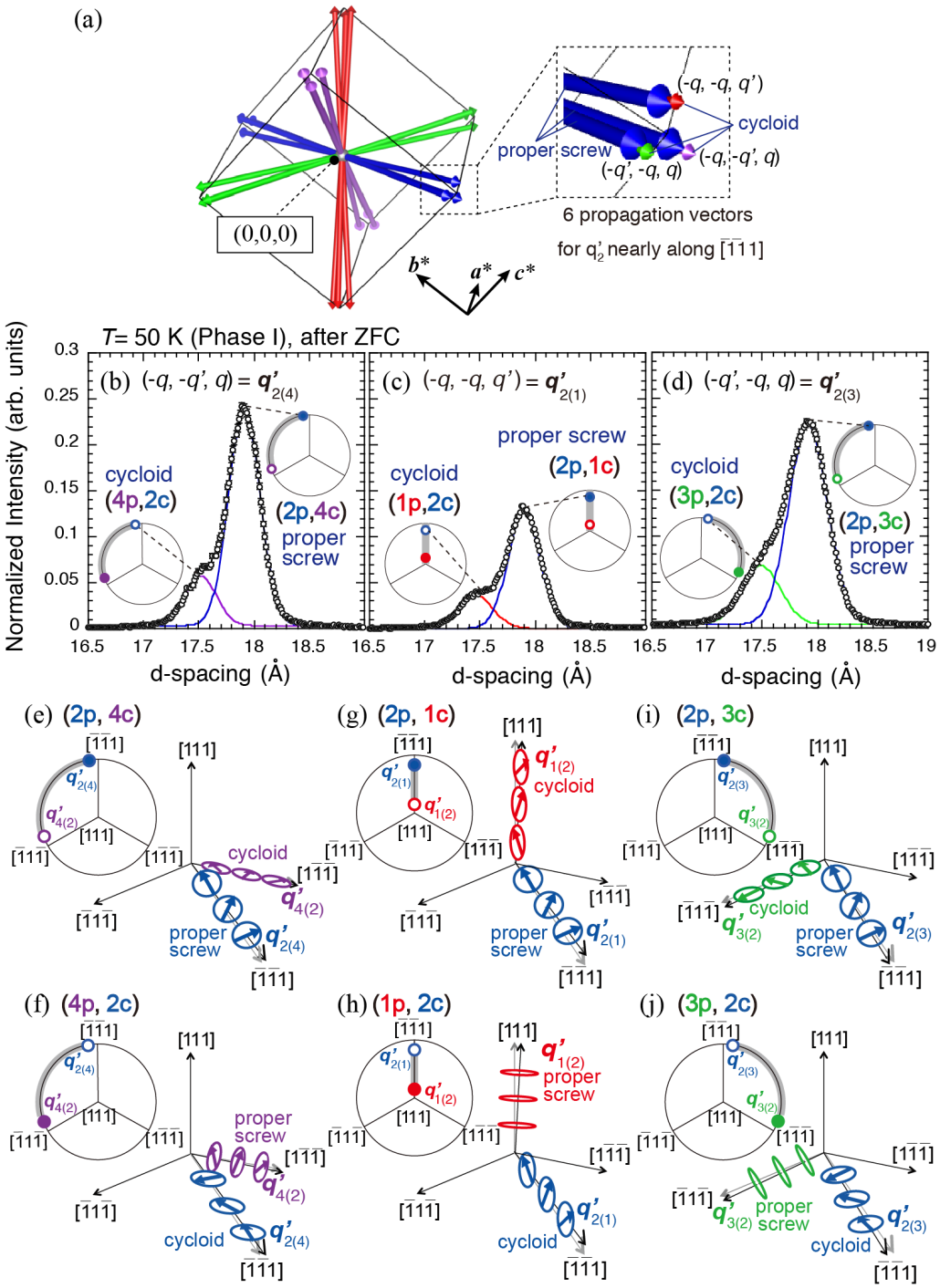

FIG. S5

(a) The schematic, showing the lengths and directions of the ***q***-vectors in Phase I after ZFC. Neutron diffraction profiles as functions of *d*-spacing for the magnetic reflections at (b) ***Q***=(−*q*, −*q*′, *q*), (c) (−*q*, −*q*, *q*′) and (d) (−*q*′, −*q*, *q*) measured at 50 K and 0 T after ZFC. The *d*-spacing, *d*, is defined as 2π/*Q*. Open circles show the normalized neutron intensity, and the solid lines are fitting curves obtained using Gaussian functions. (e-j) 6 types of ***q***-dependent domains observed by the neutron scattering for ***q***'$_2$ shown in the panels (b)-(d). Panels (e-j) correspond to the domains observed in the panels (b-d), respectively. For the name of each domain such as (2p, 4c), see Table S1.

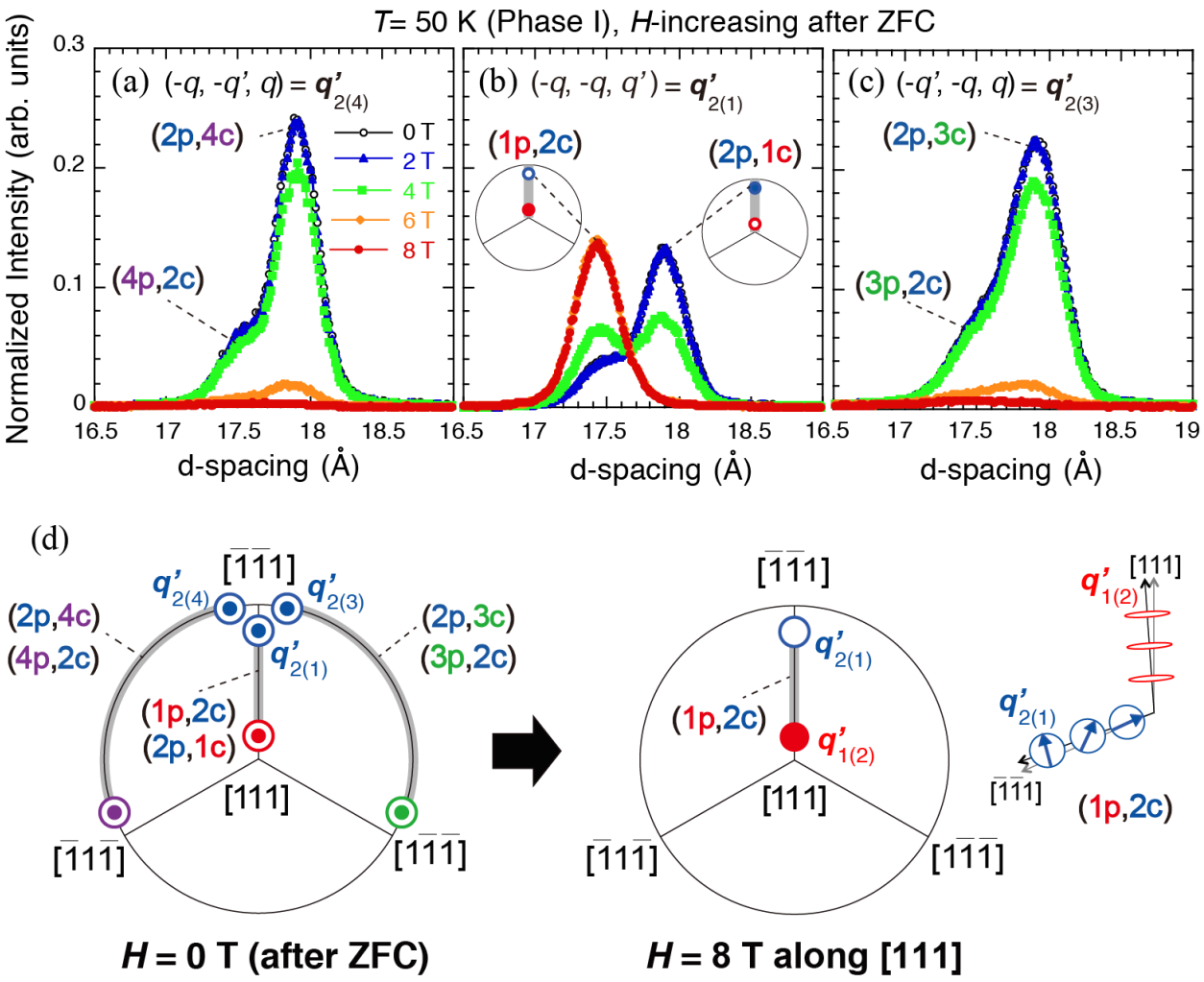

FIG. S6

Neutron diffraction profiles as functions of *d*-spacing for the magnetic reflections at (a) $\boldsymbol{Q}$=(−*q*, −*q*′, *q*), (b) (−*q*, −*q*, *q*′) and (c) (−*q*′, −*q*, *q*) measured with increasing field at 50 K after ZFC. *d*-spacing is defined as 2π/*Q*. (d) Schematic representations of double-$\boldsymbol{q}$ states at 0 T after zero-field cooling (ZFC) and that at 8 T with *H* along [111] in Phase I. The filled and open circles represent the magnetic reflections for the proper-screw and the cycloid-type spin propagation, respectively. Open circles with cores correspond to overlapping magnetic reflections of the proper-screw and the cycloid types. In each panel of (a)-(c), the doublet peaks can be found at *H* = 0 T, which correspond to each of the three circles with cores near the [-1 -1 1] direction in the panel (d). The application of an external magnetic field along [111] stabilizes the domain of (1p, 2c).

Table S1

Double-$\boldsymbol{q}$ helimagnetic domains in Phase I. "p" and "c" denote proper screw spins and cycloidal spins, respectively. There are 12 kinds of $\boldsymbol{q}$-dependent domains after ZFC. Here, the spin helicity is not considered for the number of the domain types.

	$\boldsymbol{q}'_1$ (cycloid)	$\boldsymbol{q}'_2$ (cycloid)	$\boldsymbol{q}'_3$ (cycloid)	$\boldsymbol{q}'_4$ (cycloid)
$\boldsymbol{q}'_1$ (proper screw)		(1p, 2c)	(1p, 3c)	(1p, 4c)
$\boldsymbol{q}'_2$ (proper screw)	(2p, 1c)		(2p, 3c)	(2p, 4c)
$\boldsymbol{q}'_3$ (proper screw)	(3p, 1c)	(3p, 2c)		(3p, 4c)
$\boldsymbol{q}'_4$ (proper screw)	(4p, 1c)	(4p, 2c)	(4p, 3c)	

Table S2

Symmetry elements of the anisotropic double $\boldsymbol{q}$-wave vector group and their action on $\boldsymbol{q}_1$ ($-\boldsymbol{q}_1$) and $\boldsymbol{q}_2$ ($-\boldsymbol{q}_2$).

Symmetry element	$\boldsymbol{q}_1\ (q_x^1, q_y^1, q_z^1)$	$-\boldsymbol{q}_1\ (-q_x^1, -q_y^1, -q_z^1)$	$\boldsymbol{q}_2\ (-q_x^2, -q_y^2, q_z^2)$	$-\boldsymbol{q}_2\ (q_x^2, q_y^2, -q_z^2)$
(1): x, y, z	$(q_x^1, q_y^1, q_z^1) = \boldsymbol{q}_1$	$(-q_x^1, -q_y^1, -q_z^1) = -\boldsymbol{q}_1$	$(-q_x^2, -q_y^2, q_z^2) = \boldsymbol{q}_2$	$(q_x^2, q_y^2, -q_z^2) = -\boldsymbol{q}_2$
(2; $x, -x$,0): $-y, -x, -z$	$(-q_y^1, -q_x^1, -q_z^1) = -\boldsymbol{q}_1$	$(q_y^1, q_x^1, q_z^1) = \boldsymbol{q}_1$	$(q_y^2, q_x^2, -q_z^2) = -\boldsymbol{q}_2$	$(-q_y^2, -q_x^2, q_z^2) = \boldsymbol{q}_2$
(-1; 0,0,0): $-x, -y, -z$	$(-q_x^1, -q_y^1, -q_z^1) = -\boldsymbol{q}_1$	$(q_x^1, q_y^1, q_z^1) = \boldsymbol{q}_1$	$(q_x^2, q_y^2, -q_z^2) = -\boldsymbol{q}_2$	$(-q_x^2, -q_y^2, q_z^2) = \boldsymbol{q}_2$
$(m; x, x, z)$: y, x, z	$(q_y^1, q_x^1, q_z^1) = \boldsymbol{q}_1$	$(-q_y^1, -q_x^1, -q_z^1) = -\boldsymbol{q}_1$	$(-q_y^2, -q_x^2, q_z^2) = \boldsymbol{q}_2$	$(q_y^2, q_x^2, -q_z^2) = -\boldsymbol{q}_2$